An Ancient Martian Dynamo Driven by Hemispheric Heating: Effect of Thermal Boundary Conditions

Chi Yan[1] , Ankit Barik[1] , Sabine Stanley[1,2] , Jason S.-Y. Leung[3,4] , Anna Mittelholz[5], Catherine L. Johnson[6,7],
Ana-Catalina Plesa[8], and Attilio Rivoldini[9]

[1] Department of Earth and Planetary Sciences, The Johns Hopkins University, Baltimore, MD 21218, USA; cyan10@jhu.edu
[2] The Johns Hopkins University Applied Physics Laboratory, Laurel, MD 20723, USA
[3] Department of Astronomy and Astrophysics, University of Toronto, Toronto, ON M5R 0A3, Canada
[4] Dunlap Institute for Astronomy and Astrophysics, University of Toronto, Toronto, ON M5G 2C4, Canada
[5] Department of Earth and Planetary Sciences, Harvard University, Cambridge, MA 02138, USA
[6] University of British Columbia, Vancouver, BC V6T 1Z4, Canada
[7] Planetary Science Institute, Tucson, AZ 85719, USA
[8] German Aerospace Center (DLR), Institute of Planetary Research, 12489 Berlin, Germany
[9] Royal Observatory of Belgium, 1180 Brussels, Belgium

Abstract

Magnetic field observations from the MGS, MAVEN, and InSight missions reveal that a dynamo was active in Mars's early history. One unique feature of Mars's magnetic crustal field is its hemispheric dichotomy, where magnetic fields in the southern hemisphere are much stronger than those in the northern hemisphere. Here we use numerical dynamo simulations to investigate the potential hemispheric nature of Mars's ancient dynamo. Previous studies show that a hemispheric heat flux perturbation at the core–mantle boundary could result in either a stable hemispherical magnetic field or a constantly reversing field, depending on choices of parameters used in those models. These two scenarios lead to different implications for the origin of crustal fields. Here we test the dynamo sensitivity to varying hemispheric heat flux perturbations at the core–mantle boundary in a broader parameter regime to understand whether a hemispheric dynamo is likely for early Mars. We find that features of the dynamo change from stable, hemispheric magnetic fields to reversing, hemispheric fields, with increasing hemispheric heat flux perturbations at the core–mantle boundary. We also find that magnetic fields powered by bottom heating are more stable and transition from a nonreversing, hemispheric magnetic field to a multipolar field at higher hemispheric heat flux perturbations, while the transition happens at a much lower heat flux perturbation for magnetic fields powered by internal heating.

Unified Astronomy Thesaurus concepts: Planetary interior (1248); Magnetic fields (994); Mars (1007); Magnetohydrodynamics (1964)

1. Introduction

The crustal magnetic field of Mars was first discovered by the Mars Global Surveyor (MGS) mission in 1997 (Acuña et al. 1999), later mapped by the Mars Atmosphere and Volatile EvolutioN (MAVEN) mission (Jakosky et al. 2015) and measured on the surface at the landing site of the Interior Exploration using Seismic Investigation, Geodesy and Heat Transport (InSight) mission (Banerdt et al. 2020; Johnson et al. 2020). Although no present-day dynamo-generated field was seen, global crustal magnetic fields were identified, resulting from a dynamo operating in Mars's early history.

The timing of the Martian core dynamo is constrained by various pieces of evidence. First, no substantial magnetic field anomalies are found in Mars's major impact basins (e.g., Hellas, Isidis, and Argyre) that were formed during the late heavy bombardment (LHB), suggesting that either Mars's core dynamo was inactive around 3.9 billion years ago or the crust in these basins is less capable of carrying strong magnetizations (Acuña et al. 1999; Mittelholz et al. 2020). In addition, natural remanent magnetization found in the Martian meteorite ALH84001 (Weiss et al. 2002) indicates that Mars's dynamo was active possibly during two shock events at ∼4.1 and ∼3.9 Ga (Steele et al. 2022a, 2022b). Furthermore, investigations of crustal magnetic anomalies observed in various basins, volcanoes, and lava flows on Mars demonstrate that a dynamo was operating in the pre-Noachian period (∼4.1–4.5 Ga; Acuña et al. 1999; Hood et al. 2001; Arkani-Hamed 2004; Johnson & Phillips 2005; Fassett & Head 2011; Lillis et al. 2013; Vervelidou et al. 2017) and in a younger epoch between the late Noachian and early Hesperian period (∼3.9–3.7 Ga; Lillis et al. 2008; Hood et al. 2010; Milbury et al. 2012; Mittelholz et al. 2020). Therefore, Mars's dynamo was likely active some time before the LHB (an "early dynamo"), followed by the absence of crustal magnetism observations during the LHB and then a "late dynamo" epoch around ∼3.9–3.7 Ga.

One of the most distinctive features of Mars's crustal magnetic field is its uneven distribution in the northern and southern hemispheres. Although crustal magnetic fields are observed in both hemispheres (Figure 1), the strongest magnetic fields are observed in the older Noachian terrain (especially regions around Terra Sirenum and Terra Cimmeria) in the southern hemisphere, whereas the northern hemisphere only contains weak field anomalies. In addition, no significant field anomalies can be identified in large impact basins (e.g., Isidis and Utopia in the northern hemisphere, Hellas and Argyre in the southern hemisphere), as well as over most of the large volcanic provinces.
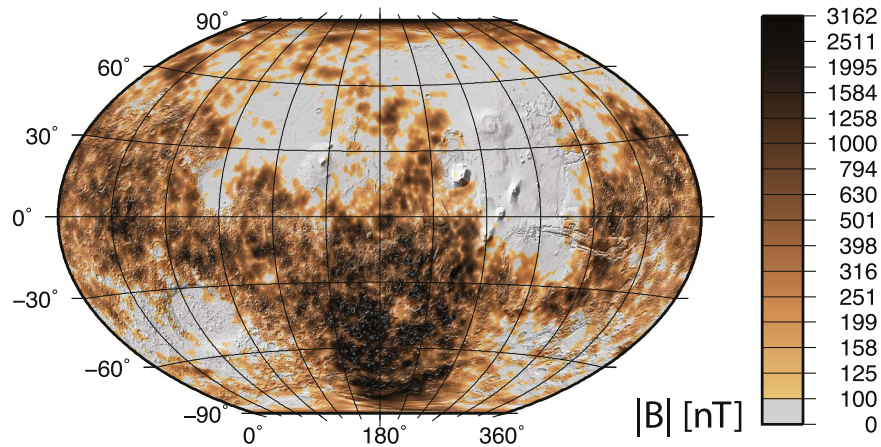
Figure 1. Map of the Martian crustal magnetic field intensity at 130 km from an Equivalent Source Dipole model (Langlais et al. 2019).
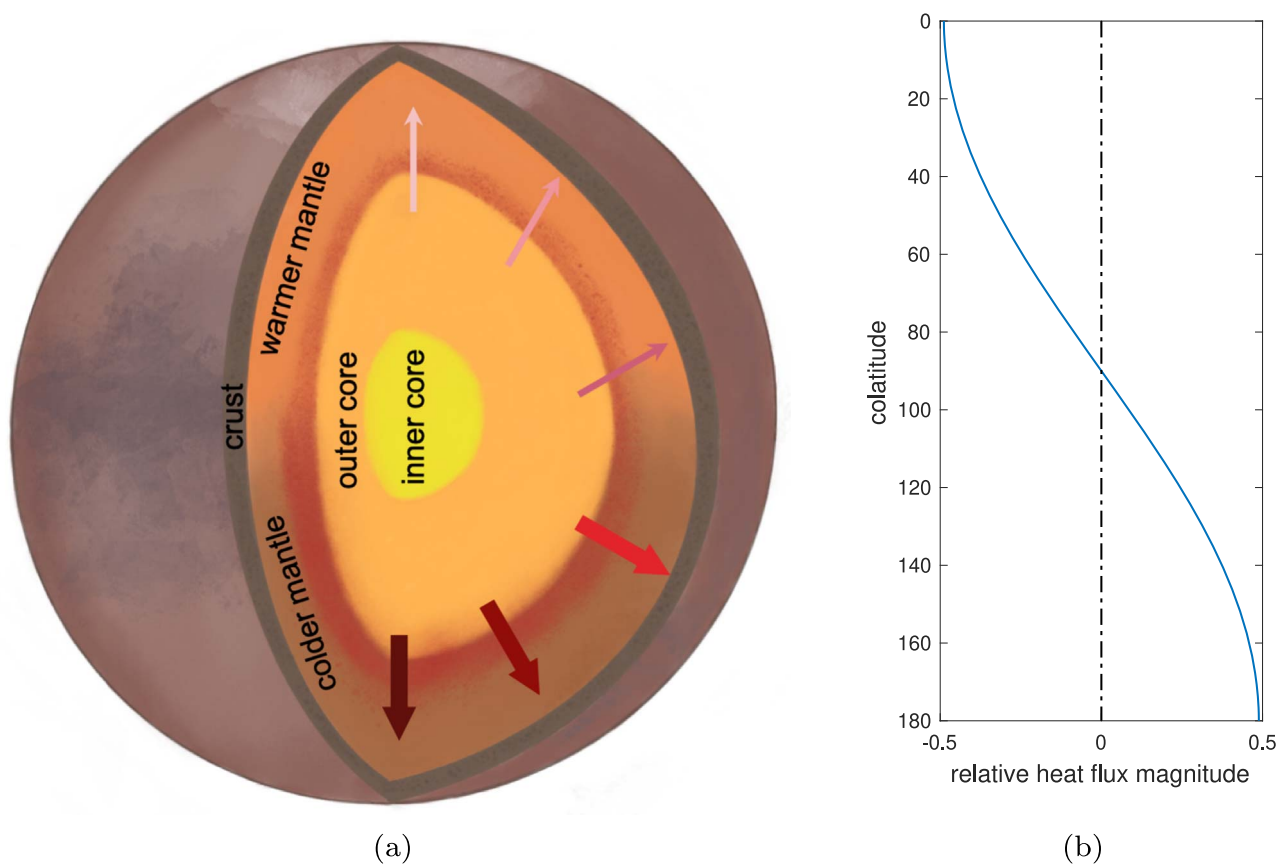

Figure 2. (a) Schematic of Mars's interior structure in our models. The heat fluxes at the southern CMB are marked by the large red arrows to represent stronger values, whereas those at the northern CMB are marked by small pink arrows representing weaker values. Darker color shades represent larger magnitudes of heat flux out of the core. (b) The Y_1^0 heat flux perturbation profile at the CMB, as a function of colatitude. Units are nondimensional.

Various theories have been proposed to explain the observed hemispheric dichotomy of the Martian crustal magnetic field. For example, large impacts can thermally or shock demagnetize the Martian crust in the absence of Mars's dynamo, resulting in a less magnetized northern hemisphere, should the northern hemisphere be preferentially bombarded (e.g., Nimmo & Gilmore 2001; Andrews-Hanna et al. 2008; Mohit & Arkani-Hamed 2004). Other studies (e.g., Solomon et al. 2005; Quesnel et al. 2009; Ojha et al. 2021) relate the concentration of the crustal magnetic field anomalies in the southern hemisphere to more extensive types of hydrothermal circulation in this region,

or to different concentrations and/or types of magnetic minerals in the different hemispheres (Mittelholz et al. 2020).

Alternatively, the hemispheric crustal magnetic field could have an internal origin, that is, due to dynamo action. Endogenic processes such as mantle circulation (e.g., Zhong & Zuber 2001; Elkins-Tanton et al. 2003, 2005; Ke & Solomatov 2006; Roberts & Zhong 2006) or exogenic processes such as impact heating (e.g., Wilhelms & Squyres 1984; Frey & Schultz 1988; Nimmo et al. 2008) can lead to a hemispheric thermal structure in the mantle, where the mantle is cooler in the southern hemisphere, therefore resulting in higher heat fluxes out of the core in the

southern hemisphere than those in the northern hemisphere (see Figure 2(a)). Stanley & Mohammadi (2008) suggest that such a hemispherically variable heat flux (VHF) perturbation pattern at Mars's core–mantle boundary (CMB), i.e., a zonal degree-one spherical harmonic (SPH) pattern Y_1^0 (i.e., degree $l = 1$, order $m = 0$; see Figure 2(b)), can result in a hemispheric dynamo producing stronger dynamo-generated magnetic fields in the southern hemisphere. It is also worth noting that in some other dynamo models hemispheric dynamos can be produced with impact-induced CMB heat flux perturbations (Monteux et al. 2015), or without invoking specific heat flow structures (Grote & Busse 2000; Simitev & Busse 2005; Landeau & Aubert 2011). The latter dynamo models operate in a specific parameter space where particular core flow modes are excited to obtain hemispheric dynamos.

Amit et al. (2011) further investigated the influence of a range of degree-one VHF perturbations, including nonzonal degree-one patterns, at the CMB on hemispheric dynamos, considering smaller magnitudes of VHF perturbations compared to those of Stanley & Mohammadi (2008). In contrast to Stanley & Mohammadi (2008), where dynamos are powered by bottom heating (BH), i.e., buoyancy sources are concentrated near the inner core boundary (ICB), dynamo models in Amit et al. (2011) are powered by internal heating (IH), where buoyancy sources are uniformly distributed within the convective core volume. They find that the observed magnetic hemispheric dichotomy on Mars can be produced with smaller VHF perturbations as long as the VHF pattern has a Y_1^0 (i.e., zonal) structure. Some of their models produce stable hemispheric dynamos similar to those in Stanley & Mohammadi (2008), whereas others produce reversing hemispheric dynamos.

Dietrich & Wicht (2013) also investigated the effects of different degree-one VHF perturbation patterns at the CMB on a dynamo model driven by IH sources. Their models involved a broader parameter regime with varying Rayleigh and Ekman numbers than the Amit et al. (2011) study. They find that their models with the Y_1^0 heat flux perturbation at the CMB produce reversing magnetic fields on timescales of ~10 kyr, and they conclude that it would be too short for undirectional magnetization in the crustal layer to explain the observed strong field anomalies in the southern hemisphere. Furthermore, studies led by Hori et al. (2012, 2014) compared the effects of various heat flux perturbations (including the Y_1^0 pattern) at the CMB on dynamo models with either BH or IH schemes. They found that, under the same level of supercriticality of Rayleigh number, the resulting intensity and field morphology of the magnetic field are more sensitive to the CMB heat flux perturbation of an internally heated dynamo model than a bottom-heated one.

This variation of dynamo behavior under the influence of the Y_1^0 VHF perturbation patterns in different studies, i.e., a stable hemispheric dynamo with magnetic fields concentrated in the southern hemisphere (Stanley & Mohammadi 2008; Amit et al. 2011) and a constantly reversing dynamo with fast reversing periods (Dietrich & Wicht 2013), suggests that there might be some fundamental mechanism that has led to these dynamo models operating in different dynamo regimes. Here we investigate whether the different heating schemes could be the major mechanism that is responsible for producing different dynamo behavior and whether the observed Martian magnetic field can be explained by a hemispheric dynamo. We focus on comparing dynamo models driven by different heating schemes

(i.e., bottom or internal) with varying magnitudes of Y_1^0 VHF perturbation at the CMB. Details of the numerical methods can be found in Section 2, results are given in Section 3, and discussions are presented in Section 4.

2. Numerical Methods

We carry out numerical dynamo simulations using the 3D magnetohydrodynamic code MagIC (Wicht 2002; Schaeffer 2013) to explore the effects of hemispheric heat flux perturbations at the CMB on the resulting magnetic field morphology, comparing different heating mechanisms. The Boussinesq approximation is employed in the models since the hydrostatic density variation across the outer core is sufficiently small for Mars. The code MagIC has been benchmarked against Christensen et al. (2001).

The code is nondimensionalized by using the shell thickness $d = r_o - r_i$ as the length scale (where r_o and r_i are the outer and inner core radii, respectively), the viscous diffusion time $\tau = d^2/\nu$ as the timescale (where ν is the kinematic viscosity), and $b = \sqrt{\rho\Omega\mu\lambda}$ as the magnetic field scale, where ρ is the constant background density, Ω is the angular velocity, μ is the magnetic permeability of free space, and λ is the magnetic diffusivity. The dimensionless momentum, magnetic induction, and thermal equations are

$$(\partial_t + \boldsymbol{u} \cdot \nabla)\boldsymbol{u} = -\nabla p - \frac{2}{E}\boldsymbol{e}_z \times \boldsymbol{u} + \frac{1}{EP_m}(\nabla \times \boldsymbol{B})$$
$$\times \boldsymbol{B} + \frac{Ra}{P_r}T\frac{\boldsymbol{r}}{r_o}, \tag{1}$$

$$\left(\partial_t - \frac{1}{P_m}\nabla^2\right)\boldsymbol{B} = \nabla \times (\boldsymbol{u} \times \boldsymbol{B}), \tag{2}$$

$$\left(\partial_t - \frac{1}{P_r}\nabla^2\right)T = -\boldsymbol{u} \cdot \nabla T + \epsilon, \tag{3}$$

as well as the equations of the Boussinesq approximation of the fluid flow and Gauss's law for magnetism:

$$\nabla \cdot \boldsymbol{u} = 0 \tag{4}$$
$$\nabla \cdot \boldsymbol{B} = 0, \tag{5}$$

where $\boldsymbol{u}$, $\boldsymbol{B}$, and T are the velocity, magnetic, and temperature fields, respectively. The parameter p is the modified pressure including the centrifugal acceleration, $\boldsymbol{e}_z$ is the unit vector in the direction of the rotation axis, and $\boldsymbol{r}$ is the position vector. The uniformly distributed buoyancy sources in the outer core are given by ϵ. The nondimensional parameters in the equations are the Ekman number, which represents the ratio of viscous to Coriolis force,

$$E \equiv \frac{\nu}{\Omega d^2}; \tag{6}$$

the Prandtl number, which represents the ratio of kinematic viscosity to thermal diffusivity κ,

$$P_r \equiv \frac{\nu}{\kappa}; \tag{7}$$

the magnetic Prandtl number, which represents the ratio of kinematic viscosity to magnetic diffusivity,

$$P_m \equiv \frac{\nu}{\lambda}; \tag{8}$$

Table 1
Nondimensional and Time-averaged Diagnostic Parameters for Bottom-heated Dynamos

Model	Ra	Nu	VHF Magnitude	R_m	Λ	$E_{\text{pol}}/E_{\text{tor}}$	Rev. Freq.
1	5.54×10^6	2.36 ± 0.04	0	84.02	0.94	0.90	...
2	5.54×10^6		0.5	91.32	1.62	0.55	...
3	5.54×10^6		1.0–4.0	...	...	...	...
4	6.56×10^6	2.57 ± 0.05	0	89.66	1.15	0.98	...
5	6.56×10^6		0.5	93.20	2.14	0.59	...
6	6.56×10^6		0.8	123.65	2.43	0.35	...
7	6.56×10^6		1.0–3.0	...	...	...	...
8	6.56×10^6		4.0	341.03	5.22	0.18	9
9	6.56×10^6		5.0	391.95	4.69	0.18	11
10	6.56×10^6		6.0	452.93	3.72	0.17	14
11	6.56×10^6		7.0	499.16	3.19	0.17	13
12	6.56×10^6		8.0	524.94	3.44	0.19	12
13	8.76×10^6	2.98 ± 0.05	0	103.38	1.52	1.09	...
14	8.76×10^6		0.5	109.59	3.42	0.57	...
15	8.76×10^6		1.0	151.79	3.71	0.36	...
16	8.76×10^6		1.5	181.03	6.80	0.19	...
17	8.76×10^6		2.0	260.36	9.09	0.12	...
18	8.76×10^6		2.5	...	...	...	...
19	8.76×10^6		3.0	404.43	2.86	0.23	6
20	8.76×10^6		4.0	473.76	0.15	0.20	10
21	8.76×10^6		5.0	540.35	0.31	0.15	13
22	1.09×10^7	3.34 ± 0.07	0	120.03	2.15	1.17	...
23	1.09×10^7		0.5	132.05	4.31	0.52	...
24	1.09×10^7		1.0	177.74	6.32	0.34	...
25	1.09×10^7		1.5	187.76	6.22	0.15	...
26	1.09×10^7		2.0–2.5	...	...	...	...
27	1.09×10^7		3.0	460.16	0.37	0.24	10
28	1.09×10^7		3.5	485.02	0.77	0.24	11
29	1.09×10^7		4.0	540.45	0.26	0.17	15
30	1.4×10^7	3.81 ± 0.08	0	131.65	2.20	1.13	...
31	1.4×10^7		0.5	141.08	4.99	0.53	...
32	1.4×10^7		1.0	187.39	7.70	0.35	...
33	1.4×10^7		1.5	262.41	11.79	0.15	...
34	1.4×10^7		2.0	...	...	...	...
35	1.4×10^7		2.5	480.50	0.13	0.28	11
36	1.4×10^7		3.0	520.81	0.25	0.25	13
37	1.4×10^7		4.0	615.61	0.47	0.22	14
38	1.62×10^7	4.1 ± 0.09	0.0	142.12	2.38	1.11	...
39	1.84×10^7	4.38 ± 0.1	0.0	152.48	2.65	1.09	...
40	2.05×10^7	4.1 ± 0.09	0.0	161.39	2.83	1.10	...
41	2.27×10^7	4.62 ± 0.11	0.0	172.60	2.99	1.03	...
42	2.50×10^7	4.86 ± 0.11	0.0	179.60	3.30	1.01	...
43	2.80×10^7	5.47 ± 0.13	0.0	194.36	3.29	0.99	...
44	3.50×10^7	6.09 ± 0.18	0.0	306.41	2.06	0.51	Δ
45	4.00×10^7	6.51 ± 0.18	0.0	308.34	2.31	0.56	Δ

Note. The Ekman, Prandtl, and magnetic Prandtl numbers are held fixed at $E = 9.5 \times 10^{-5}$, $\boldsymbol{Pr} = 1$, and $\boldsymbol{Pm} = 1$. $R_m \equiv UL/\lambda$, i.e., the magnetic Reynolds number where U (L) is the characteristic velocity (length) scale of the flow. $\Lambda \equiv \sigma \boldsymbol{B}^2/\rho\Omega$ is the Elsässer number of the rms field in the fluid outer core that evaluates the ratio of the magnetic force to the Coriolis force, where σ is the electrical conductivity. $E_{\text{pol}}/E_{\text{tor}}$ is the ratio of the poloidal to toroidal magnetic energy of the rms field in the fluid outer core. "Rev. Freq." gives the rounded number of reversals per one magnetic diffusion time ($\tau_m = 2\pi Pm/\tau$) if the magnetic dipole field is reversing. Nonreversing, dipolar-dominated field is denoted by ellipses, aperiodically reversing field is denoted by "AP," and multipolar fields generated with homogeneous heat flux boundaries are marked by "Δ." Decaying fields are marked with ellipses in the R_m and Λ columns.

and the Rayleigh number, which represents the vigor of buoyancy forces driving convection relative to dissipative forces,

$$\text{Ra} \equiv \frac{g_0 d^3}{\nu\kappa} T_{\text{scale}}, \qquad (9)$$

where g_0 is the gravitational acceleration at the CMB and $T_{\text{scale}} = q_0 d/\rho_0 C_p \kappa$ is the temperature scale, in which q_0 is the mean heat flux at the CMB and C_p is the specific heat capacity.

We vary the Rayleigh number to simulate various levels of buoyancy forcing while the other nondimensional parameters, i.e., the Ekman, Prandtl, and magnetic Prandtl, are held fixed for all models. See note to Table 1 for numeric values.

We investigate two end-member heating schemes, i.e., BH and IH, to evaluate their effects on the magnetic field morphologies. The core of a planet must cool sufficiently to sustain a planetary core dynamo. The energy to drive the core can arise from multiple sources, such as the secular cooling of the core, energy from the decay of radioactive elements within

Table 2
Nondimensional and Diagnostic Parameters for Internally Heated Dynamos

Model	Ra	Nu	VHF Magnitude	R_m	Λ	$E_{\mathrm{pol}}/E_{\mathrm{tor}}$	Rev. Freq.
46	1.09×10^7	1.86 ± 0.04	0	58.79	1.27	1.03	⋯
47	1.09×10^7		0.5	144.31	0.60	0.34	AP
48	1.09×10^7		1.0	⋯	⋯	⋯	⋯
49	1.09×10^7		1.5	248.14	8.33	0.33	6
50	1.09×10^7		2.0	374.18	0.15	0.26	8
51	1.09×10^7		2.5	418.45	0.30	0.21	10
52	1.09×10^7		3.0	455.82	0.38	0.20	11
53	1.4×10^7	2.16 ± 0.06	0	68.87	1.71	0.96	⋯
54	1.4×10^7		0.5	137.57	6.15	0.13	⋯
55	1.4×10^7		1.0	257.92	8.46	0.06	⋯
56	1.4×10^7		1.5	363.21	0.15	0.30	8
57	1.4×10^7		2.0	419.97	0.28	0.24	11
58	1.4×10^7		2.5	512.98	0.68	0.17	11
59	1.4×10^7		3.0	548.84	1.03	0.16	9
60	1.91×10^7	2.61 ± 0.09	0	83.05	2.03	1.21	⋯
61	1.91×10^7		0.5	168.97	7.14	0.13	⋯
62	1.91×10^7		1.0	341.31	0.18	0.35	10
63	1.91×10^7		1.5	424.73	0.30	0.27	9
64	1.91×10^7		2.0	492.62	0.40	0.24	11
65	2.29×10^7	2.88 ± 0.07	0	91.05	2.41	1.21	⋯
66	2.29×10^7		0.5	178.68	7.88	0.14	⋯
67	2.29×10^7		1.0	373.98	0.26	0.33	10
68	2.29×10^7		1.5	457.76	0.47	0.26	10
69	2.29×10^7		2.0	527.76	0.80	0.21	10
70	3.06×10^7	2.99 ± 0.1	0	184.66	0.64	0.48	△
71	$\mathbf{3.5 \times 10^7}$	3.2 ± 0.09	0	210.00	0.70	0.46	△

Note. See Table 1 for parameter definition.

the core, tidal forcing, the latent heat produced as the inner core solidifies, and the compositional energy as the light elements are released at the ICB. The last two energy sources, considered as BH, are associated with the inner core growth and concentrated near the ICB. IH can refer to the radioactive decay and sometimes tidal forcing for particular planetary bodies where buoyancy is distributed within the convective core.

Since the convective driving force for Mars's ancient dynamo is unknown, we explore both heating mechanisms. In our study, we assume that energy is conserved in the core, i.e., no heat is built up or lost from the core dynamo region. For bottom-heated cases, the heat flow at the CMB, Q_{CMB}, is balanced by the heat flow at the ICB, Q_{ICB}, i.e., $Q_{\mathrm{CMB}} = Q_{\mathrm{ICB}}$. For internally heated cases, we have no heat flow at the ICB and the CMB heat flow is balanced by the heat generated through the uniform volumetric heating source ϵ within the core, i.e., $Q_{\mathrm{CMB}} = P_r \frac{4}{3}\pi(r_o^3 - r_i^3)\epsilon$.

We then further implement a zonal, degree-one SPH pattern Y_1^0, superimposed on a homogeneous CMB heat flux background, to explore the effects of Mars's lower mantle thermal heterogeneity on dynamo action. With this modulation of the Y_1^0 VHF perturbation, minimum (maximum) heat fluxes are expected out of the northern (southern) hemisphere at the CMB (Figure 2(b)). We vary the strength of heat flux perturbation at the CMB by the variable VHF magnitude, which gives the maximum difference of heat flux perturbation at the CMB $|\Delta q|_{\mathrm{max}}$. This can further be related to q^* defined in Amit et al. (2011) by VHF magnitude $= 0.58q^*$.

Although the latest tidal and seismic studies from InSight measurements (Konopliv et al. 2020; Stahler et al. 2021; Khan et al. 2022) suggest that the core may be fully liquid owing to

the presence of significant light elements (Terasaki et al. 2019), a small inner core with a radius ratio $r_i/r_o = 0.35$ is adopted in this study in order to directly compare with previous dynamo studies (Stanley & Mohammadi 2008; Amit et al. 2011; Dietrich & Wicht 2013). We assume that the inner core is electrically insulating to minimize its effects on the magnetic field. Both boundaries (the ICB and the CMB) are stress-free, are electrically insulating, and have a fixed heat flux boundary condition.

We use spectral methods with 65 Chebyshev polynomials in the radial direction. Scalars on each spherical surface are resolved in latitude and longitude using spherical harmonics with maximum degree and order 170. Each numerical simulation has been run at least a few viscous diffusion times after equilibrium. Time-averaged values refer to values that are time-averaged over one viscous diffusion time after the dynamo models have been equilibrated. The input model and time-averaged diagnostic parameters in our simulations are listed in Table 1 for bottom-heated models and Table 2 for internally heated models.

3. Results

We begin our investigation of different heating mechanisms by analyzing our control models, where the heat flux at the CMB is homogeneous, i.e., models 1, 4, 13, 22, 30, and 38–45 for bottom-heated dynamos and models 46, 53, 60, 65, and 70 for internally heated ones (Tables 1 and 2). Figure 3(a) illustrates the representative magnetic field morphology produced by these control models, where the radial magnetic field is dominated by a nonreversing axial dipole component. The time-averaged fluid flows generated by models with homogeneous heat flux boundaries show some representative
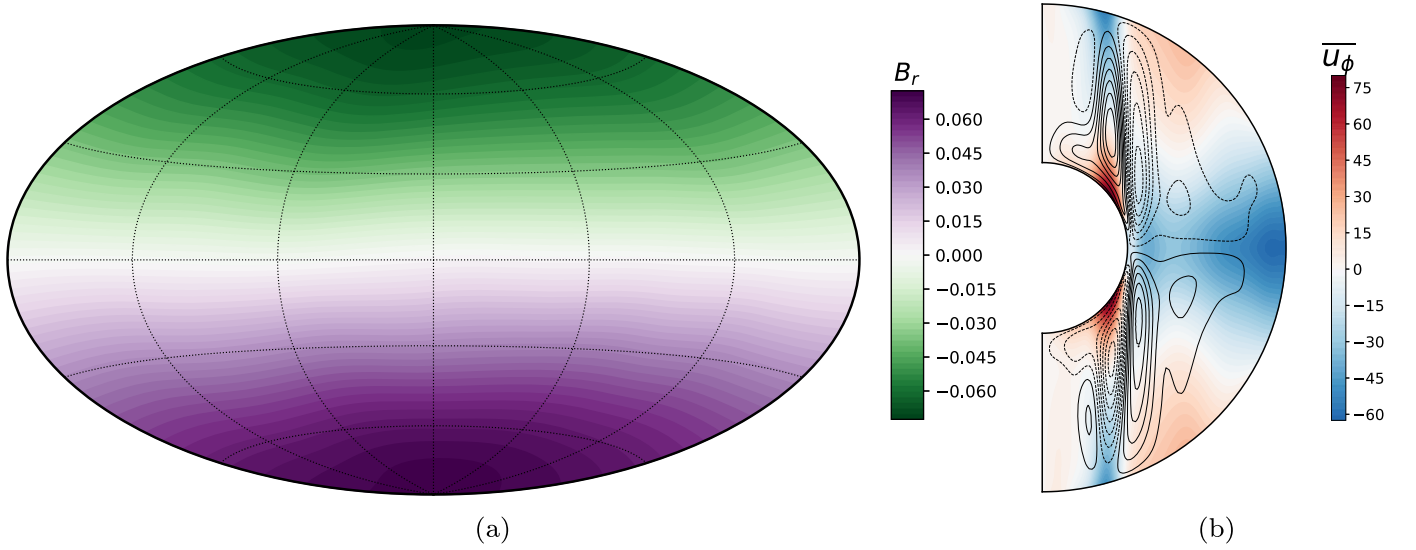
Figure 3. Dynamo images of a dipolar-dominated BH control model 13: (a) a snapshot of the radial magnetic field extrapolated to the surface r_S, where $r_o/r_S = 0.54$, and (b) filled contours of the time-averaged axisymmetric zonal flows ($\overline{u_\phi}$) and streamlines of meridional circulation in the outer core. The solid streamlines represent clockwise flows, while the dashed streamlines are counterclockwise flows. Units are nondimensional.

fluid motions in the outer core, including the equatorial upwellings and downwellings at the tangent cylinder drawn by the presence of the inner core, as well as the westward zonal flows around the low latitudes (Figure 3(b)). These features of the fluid flows near the tangent cylinder would not be expected in full sphere dynamos without a solid inner core. The zonal flows are approximately equatorially symmetric, while meridional flows are equatorially antisymmetric.

However, there are some differences in the flow structures of these control cases between the bottom-heated and internally heated dynamo models. In Figure 4 we compare two control models (BH model 13 and IH model 65) that have the same relative convective heat transfer across the dynamo region, i.e., the same Nusselt number (i.e., $Nu = \frac{\Delta T_c}{\Delta T}$, where ΔT_c is the temperature difference created by the fixed conductive heat flux across the shell and ΔT is the true temperature difference across the shell). We can see that the radial flows in the bottom-heated control case (model 13, Figure 4(a)) are stronger closer to the inner core and diffused near the CMB, whereas those in the internally heated control model (model 65, Figure 4(c)) are stronger toward the CMB. The distribution of the poloidal kinetic energy over the outer core radii further illustrates that the poloidal kinetic energy of the bottom-heated control model (Figure 4(b)) is concentrated in longer wavelengths (i.e., SH l from 3 to 10) and close to the inner core (i.e., within $r = 1.0$), while for the internally heated control case (Figure 4(d)) it is concentrated in shorter wavelengths (i.e., SH l from 6 to 40) and throughout the core (r from 0.8 to 1.4).

Next, we investigate the magnetic morphology by comparing the dipole dominance of our control models with varying Rayleigh numbers. In Figure 5 we plot the dipolarity f_{Dip} (Christensen & Aubert 2006), defined as

$$f_{\mathrm{Dip}} = \left[\frac{\int_S \boldsymbol{B}_1^0(r=r_o) \cdot \boldsymbol{B}_1^0(r=r_o)dS}{\int_S \sum_{l=1} \boldsymbol{B}_l(r=r_o) \cdot \boldsymbol{B}_l(r=r_o)dS} \right]^{1/2}, \quad (10)$$

where S represents the surface of the CMB, against the local Rossby number Ro_l (Christensen & Aubert 2006),

$$Ro_l = \frac{U}{\Omega d} \frac{\overline{l_u}}{\pi}, \quad (11)$$

where $\pi/\overline{l_u}$ is the characteristic half-wavelength of the velocity field and $\overline{l_u}$ is derived from the time-averaged kinetic energy spectrum,

$$\overline{l_u} = \frac{\sum l \langle \boldsymbol{u}_l \cdot \boldsymbol{u}_l \rangle}{2E_{\mathrm{kin}}}, \quad (12)$$

Here $\boldsymbol{u}_l$ represents velocity at degree l and E_{kin} is the kinetic energy integrated in the entire volume:

$$E_{\mathrm{kin}} = \frac{1}{2} \int_V v^2 dV. \quad (13)$$

As the Rayleigh number increases, the local Rossby number increases, and dynamo models transition from a nonreversing, dipolar-dominated (i.e., $f_{\mathrm{Dip}} > 0.35$) field to a multipolar (i.e., $f_{\mathrm{Dip}} \leqslant 0.35$) field at particular local Rossby numbers. We find that this transition happens at different critical local Rossby numbers for models powered by different heating mechanisms (Figure 5). For bottom-heated models, the critical local Rossby number is 0.1, consistent with previous studies (e.g., Olson & Christensen 2006). However, for internally heated dynamos, the transition happens at $Ro_l \sim 0.06$, a comparatively smaller local Rossby number. This suggests that the critical length scale determining the dipolar-dominant to multipolar magnetic field transition of internally heated models is almost half the value as for bottom-heated dynamos. Furthermore, as the local Rossby number increases, the dipolarity of magnetic fields produced by internally heated control models decreases more rapidly than that by bottom-heated models. This further indicates a comparatively narrower window in the choice of Rayleigh numbers for internally heated dynamos to produce dipolar-dominated magnetic fields than for bottom-heated dynamos. In our studies, the Rayleigh numbers of internally
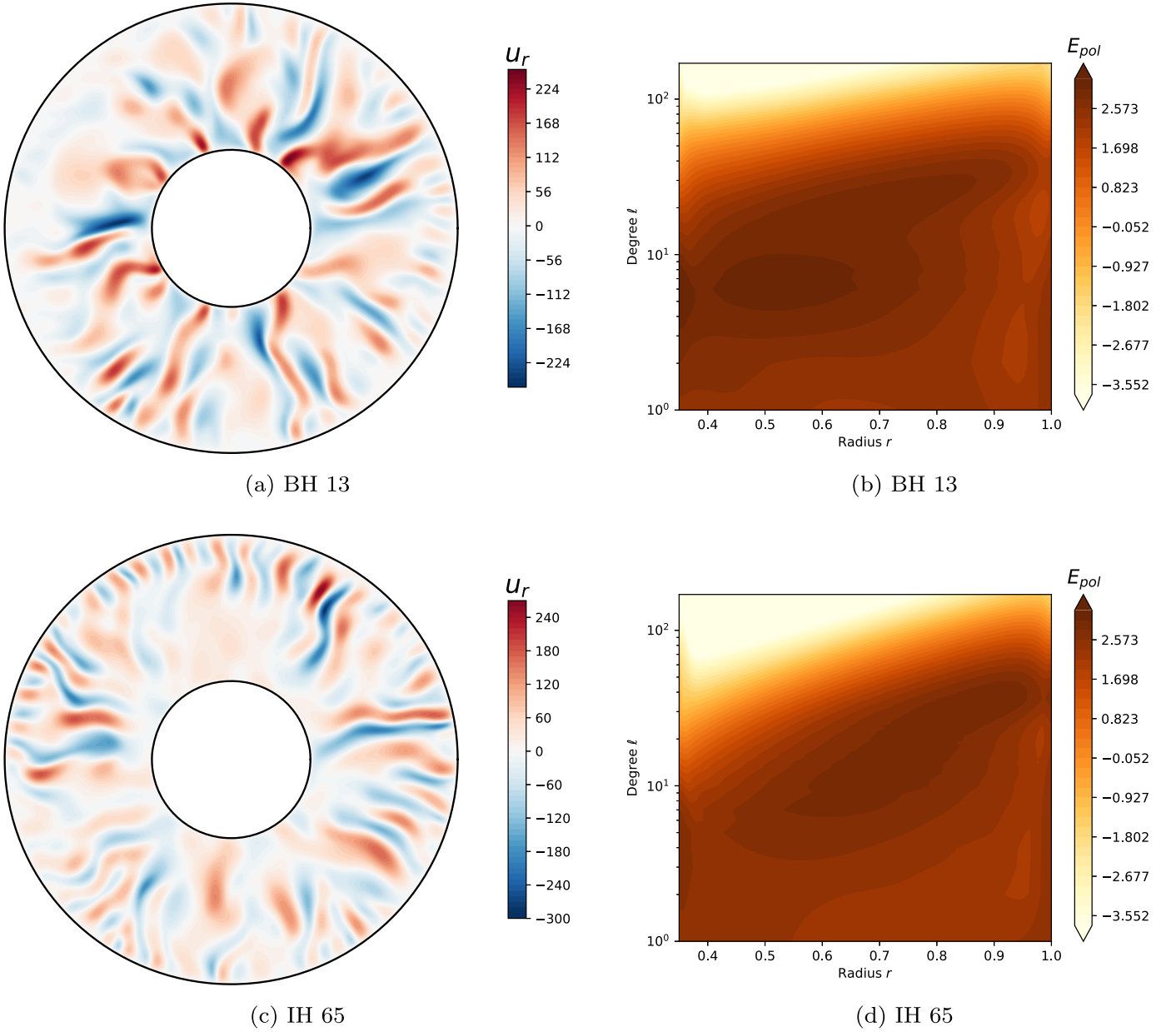
(a) BH 13

(b) BH 13

(c) IH 65

(d) IH 65

Figure 4. Snapshots of the radial velocities in the equatorial plane of the BH control model 13 (panel (a)) and IH control model 65 (panel (c)) in nondimensional units. Time-averaged poloidal kinetic energy spectrum distribution in the outer core (where $r_i = r_{io}/(1 - r_{io}) = 0.538$ and $r_o = 1/(1 - r_{io}) = 1.538$) of the BH control model 13 (panel (b)) and the IH control model 65 (panel (d)), shown in logarithmic scale. Values in the color bar represent the base-10 logarithmic values of the kinetic energy.

heated control models that produce dipolar-dominated fields range from $\sim$7Ra$_c$(int) to 15Ra$_c$(int), while those of bottom-heated dynamo models range from $\sim$23Ra$_c$(bot) to 116Ra$_c$(bot), where Ra$_c$(int) $= 1.53 \times 10^6$ is the critical Rayleigh number for internally heated models and Ra$_c$(bot) $= 2.42 \times 10^5$ for bottom-heated models. Thus, the range of Rayleigh number of bottom-heated dynamos able to produce dipolar-dominated fields is about 43% wider than that of internally heated dynamo models. For the remainder of this study, we only consider cases with Rayleigh numbers for which control models produced dipolar fields.

We then start to apply the Y_1^0 VHF perturbation pattern at the CMB in our dynamo models, which leads to a more hemispheric magnetic field. In Figure 6 we show as an example the surface radial magnetic field, which is concentrated in the southern

hemisphere. The most vigorous convection rolls are located in the southern hemisphere, as the Y_1^0 VHF perturbation pattern makes the southern CMB colder.

To evaluate the level of hemisphericity of our dynamo models, we define the hemisphericity of the surface magnetic field (H_{sur}) as the ratio of the surface integrals of the time-averaged magnetic field intensities in the southern and northern hemispheres:

$$H_{sur} = \left[\frac{\int_{\pi/2}^{\pi} \int_0^{2\pi} |\langle \boldsymbol{B} \rangle|^2 \sin \theta d\theta d\phi}{\int_0^{\pi/2} \int_0^{2\pi} |\langle \boldsymbol{B} \rangle|^2 \sin \theta d\theta d\phi} \right]^{1/2}, \qquad (14)$$

where $\langle \rangle$ denotes time average and the magnetic field $\boldsymbol{B}$ is evaluated at the surface of Mars (r_S) by upward continuing the magnetic field from the CMB r_o to the surface using
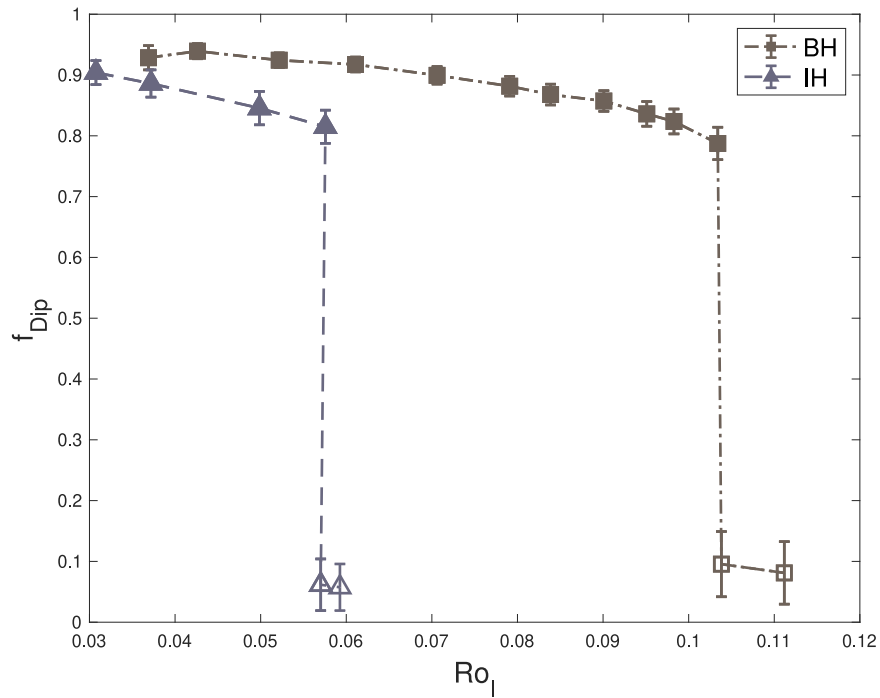
Figure 5. The relation between dipolarity and the local Rossby number for BH and IH control cases. Filled/open symbols represent nonreversing/reversing models, respectively.
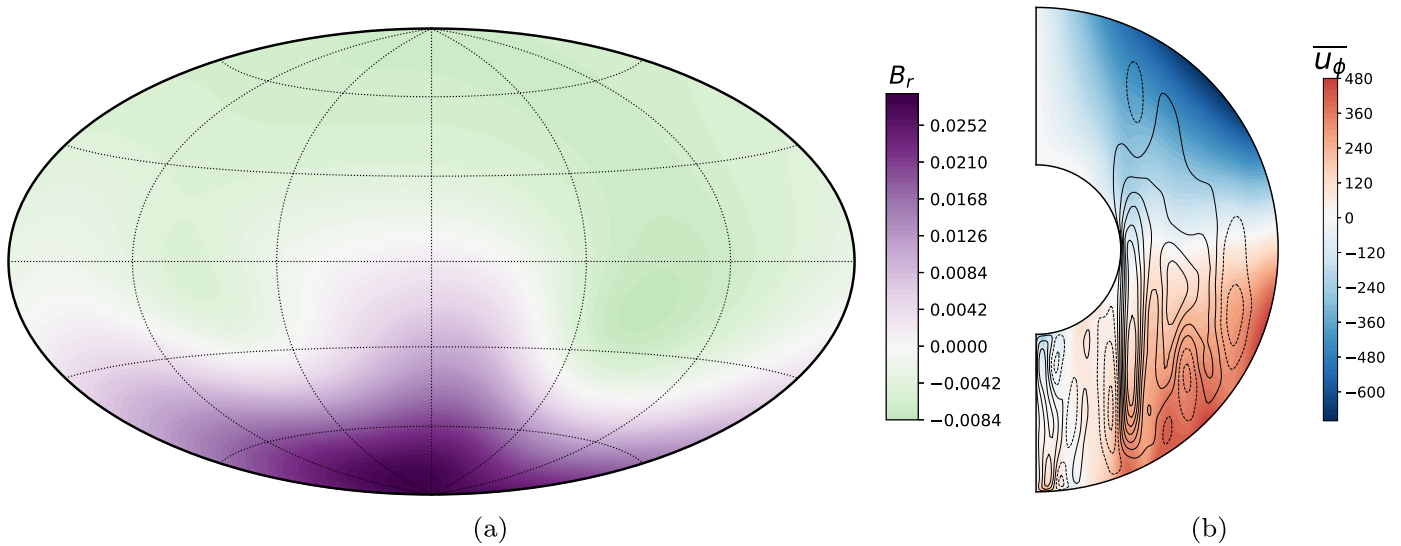

Figure 6. Dynamo images of a hemispheric dynamo model 25: (a) a snapshot of the radial magnetic field at the surface; (b) filled contours of time-averaged zonal flows ($\overline{u_\phi}$) and streamlines of meridional circulation in the outer core. The solid streamlines represent clockwise flows, while the dashed streamlines are counterclockwise flows. Units are nondimensional.

$r_o/r_S = 0.54$. The resulting hemisphericities for all models are shown in Figure 7.

First of all, it can be seen from Figure 7 that the time-averaged hemisphericity is equal to 1 (i.e., $H_{sur} = 1$) for bottom-heated and internally heated control models (i.e., models 1, 4, 13, 22, and 30 in Table 1 and models 46, 53, 60, and 65 in Table 2) with homogeneous heat flux (i.e., VHF magnitude = 0), where the resulting magnetic fields are nonreversing and dipolar dominated. Second, at a relatively small magnitude of the VHF perturbation (i.e., VHF ⩽ 2 for BH models and VHF ⩽ 1 for IH models; filled symbols in Figure 7), the resulting magnetic field is nonreversing and

dipolar dominated for all bottom-heated and internally heated dynamo models, except one internally heated case (i.e., model 47 in Table 2), which produces an aperiodically reversing, dipolar-dominated magnetic field. At these small VHF perturbation magnitudes, models with higher Rayleigh number yield mildly higher hemisphericity. In addition, at the smallest non-zero case we considered (VHF magnitude = 0.5), the averaged H_{sur} produced by internally heated models with varying Rayleigh numbers ($H_{sur} = 1.32 \pm 0.06$) is slightly higher than that produced by bottom-heated models ($H_{sur} = 1.14 \pm 0.02$), suggesting that IH models are more sensitive to VHF perturbations in producing hemispheric fields.

8

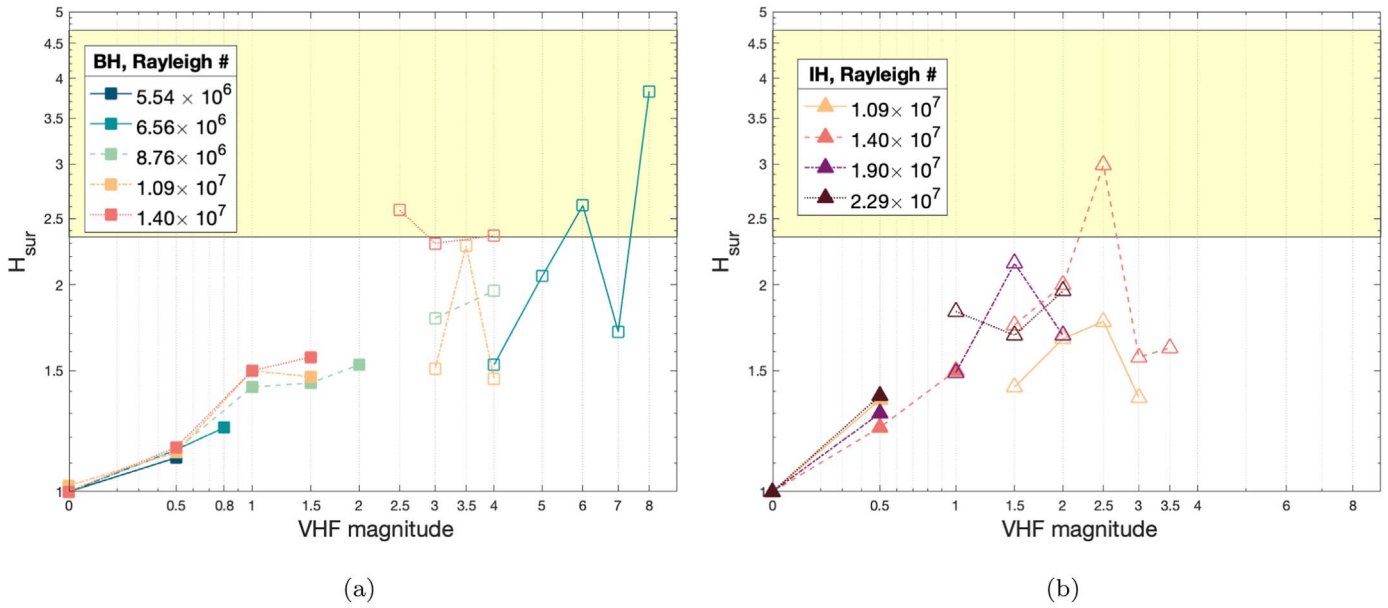**Figure 7.** Time-averaged magnetic hemisphericity H_{sur} at the surface of models with varying Rayleigh numbers and Y_1^0 VHF perturbation magnitude for (a) BH and (b) IH models. Squares (triangles) represent BH (IH) cases, whereas open (filled) symbols represent nonreversing (reversing) models. The yellow shaded region represents the estimated Mars crustal magnetic field dichotomy ratio (Amit et al. 2011). Breaks in the lines are provided for visual clarity to show where the field transitions from the dipolar-dominated to multipolar regime. Different colors represent dynamo models with different Rayleigh numbers. Both axes are on logarithmic scales.

This difference disappears at VHF = 1.0, where similar H_{sur} values are produced by two different heating mechanisms.

We then further compare two models at the same level of heat flux perturbation (VHF = 0.5) but powered by different heating mechanisms, i.e., the internally heated model 66 and the bottom-heated model 14. These two models are chosen so that their corresponding control models (i.e., IH model 65 and BH model 13) have the same Nusselt number. Figure 8 highlights different dynamic effects brought by different heating mechanisms. First, there are fewer convection cells (Figure 8(a)) in the BH model 14 compared to those in the BH control model 13 (Figure 4(a)). Furthermore, it can be seen that radial flows are localized closer to the inner core ($r < 1.0$), with the poloidal kinetic energy concentrated within SH degrees $l = 1-7$, compared to the homogeneously BH control model 13 (Figure 4(b)). In contrast, the radial flows in the IH model 66 are concentrated around the outer part of the fluid core (r from 1.2 to 1.4), with the poloidal kinetic energy constrained to a narrower range of length scales (SH degrees $l = 10-20$), compared with the IH control model 65 (Figure 4(d)).

It is worth noting that an internally heated dynamo model 47 produces an aperiodically reversing (Figure 9(a)) magnetic field with dipole dominance ($f_{dip} = 0.53 \pm 0.18$) at 0.5 VHF perturbation magnitude. The magnetic field stays hemispheric with fields concentrated in the southern hemisphere mostly (i.e., $H_{sur} > 1.0$) during both polarities, while minimal hemisphericities (i.e., $H_{sur} < 1.0$, which implies stronger fields in the northern hemisphere) are found during the event of dipole reversals or large excursions (Figure 9(b)). Therefore, the time-averaged magnetic hemisphericity is still moderately high ($H_{sur} = 1.36$), since the time interval of field reversals or excursions is relatively short.

As the Y_1^0 VHF perturbation magnitude increases, the dynamo behavior of models with different heating mechanisms further diverges. For bottom-heated models, the resulting magnetic field becomes more hemispheric with increasing

VHF perturbation magnitude, while the field stays dipolar dominated and nonreversing, until a critical VHF perturbation magnitude is reached, after which the dynamo decays. However, at a higher VHF perturbation magnitude, the dynamo then resurrects into a multipolar field with a frequently reversing dipole component (Figure 7(a)).

For internally heated dynamos, the resulting magnetic field transitions from a nonreversing, dipolar-dominated to a multipolar field at much smaller VHF perturbation magnitudes than those of bottom-heated models. Additionally, this transition between different magnetic field morphologies happens more smoothly for internally heated dynamos. We did not see any dynamo cessation in the internally heated models we explored, except for models with Ra = 1.09×10^7.

The reason for the dynamo cessation can be found in the deconstruction of the magnetic energy (Figure 10). Here we calculated the magnetic energy summed up by its poloidal and toroidal components in the outer core volume:

$$E_B = E_{pol} + E_{tor}$$
$$= \frac{1}{2} \int_V (\boldsymbol{B}_p^2 + \boldsymbol{B}_t^2) dV. \quad (15)$$

Shown in Figures 10(a) and (b) is the magnetic energy integrated in the outer core for all dynamo models with various VHF perturbation magnitudes. We can see that in the control models with VHF = 0, initially, both bottom-heated and internally heated models have the same magnitude of magnetic energy, with a poloidal-to-toroidal ratio (E_{pol}/E_{tor}) around unity. Then, as the VHF perturbation magnitude increases, the magnetic energy increases, while the poloidal-to-toroidal ratio decreases to a minimum. In order to maintain the dynamo action, there should be sufficient poloidal and toroidal magnetic field. For all the BH models, a critical VHF magnitude is reached at which the dynamo decays. As the VHF magnitude is increased beyond this decay value, another critical VHF
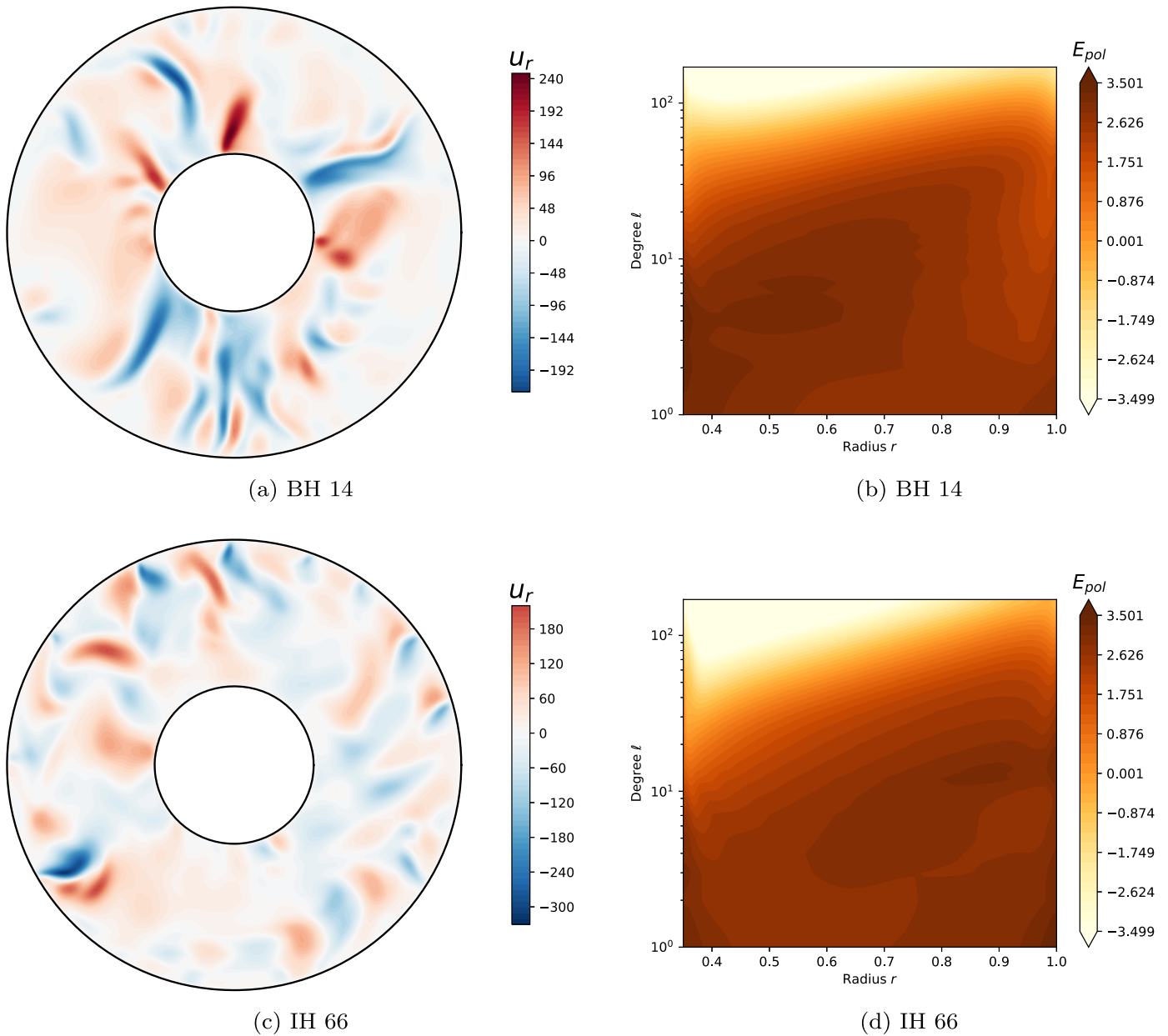
Figure 8. Snapshot of the radial velocities in the equatorial plane of the BH model 14 (panel (a)) and the IH model 66 (panel (c)) in nondimensional units. Time-averaged poloidal kinetic energy spectrum distribution in the outer core ($r_i = 0.538$ and $r_o = 1.538$) of the BH model 14 (panel (b)) and the IH model 66 (panel (d)), shown in logarithmic scale. Values in the color bar represent the base-10 logarithmic values of the kinetic energy.

magnitude is reached at which the dynamo revives from a decaying field but produces a multipolar magnetic field. For the IH models, a decaying dynamo was only found for the case with the lowest Rayleigh number in our study. However, the transition to a multipolar magnetic field regime at a critical VHF also occurs.

It can be seen from Figures 10(a) and (b) that the magnetic energy in the multipolar regime has decreased by two orders of magnitude, compared with the magnetic energy just before the critical transition point. For example, for bottom-heated models with $Ra = 8.76 \times 10^6$, the magnetic energy drops down to 0.3% when the dynamo first transitions to the multipolar magnetic field at VHF = 2.5, compared with the total magnetic energy at VHF = 1.5 perturbation magnitude.

In the multipolar magnetic field regime, the total magnetic energy increases with the increasing Y_1^0 VHF perturbation

magnitude. Interestingly, by comparing models with the same Rayleigh number, the magnetic energy is always smaller than the energy of the homogeneously heated control case in the nonreversing, dipolar-dominated regime. For example, the largest magnetic energy in the multipolar field regime (model 21) in bottom-heated models with $Ra = 8.76 \times 10^6$ is 64% of the magnetic energy in the homogeneously heated control case (model 13). Furthermore, both bottom-heated and internally heated models transition into the multipolar field regime at a much smaller poloidal-to-toroidal ratio, and then as the Y_1^0 VHF perturbation magnitude increases, this ratio gradually decreases and saturates at a steady ratio. For bottom-heated models the poloidal-to-toroidal ratio restarts at $23\% \pm 4\%$ and saturates to $18\% \pm 3\%$ in the multipolar regime, whereas for internally heated models this poloidal-to-toroidal ratio is slightly higher,
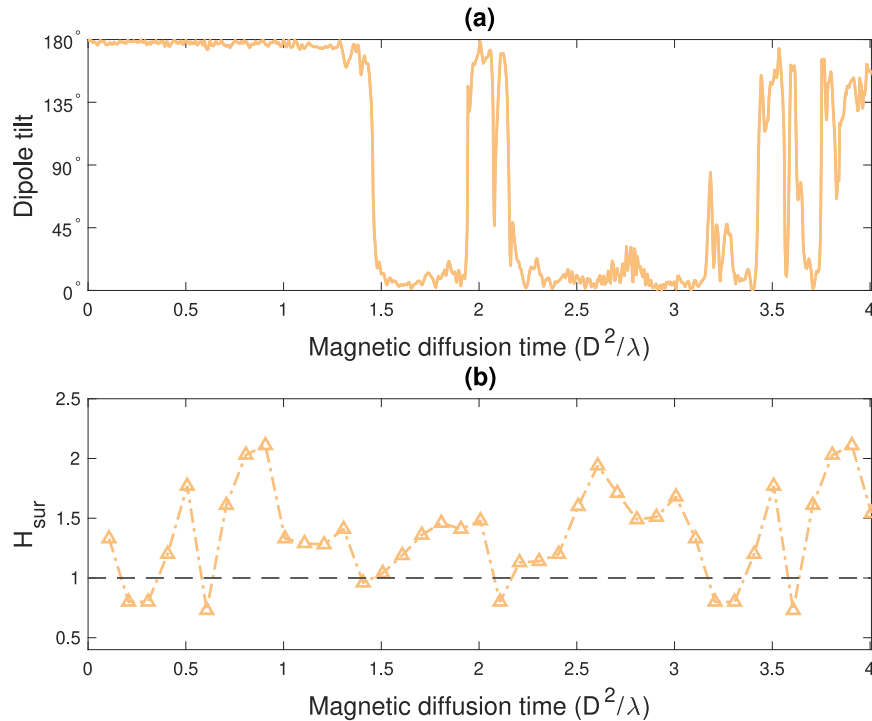
Figure 9. The time series of the dipole tilt (panel (a)) and the magnetic hemisphericity (panel (b)) of the internally heated model 47. The dashed line in panel (b) represents no magnetic hemisphericity, i.e., $H_{sur} = 1$.

$E_{pol}/E_{tor} = 33\% \pm 2\%$, when the field becomes multipolar and saturates to $20\% \pm 3\%$.

In the multipolar regime, the time-averaged hemisphericity varies with increasing VHF magnitude for both bottom-heated and internally heated dynamos (Figure 7). Because the magnetic hemisphericity is smallest during reversals or large excursions, too frequent field reversals can lower the time-averaged hemisphericity value. Therefore, the resulting hemisphericity depends on the number of reversals and excursions in the averaged time frame. For instance, excluding the measured hemisphericity values at reversals and excursions for the internally heated model 68, the resulting hemisphericity value is $H_{sur} = 2.03$, comparatively higher than the hemisphericity value including all times. Additionally, it is also worth noting that all resulting hemisphericities in the multipolar field regime are still higher than 1, indicating that more magnetic fields are concentrated in the southern hemisphere, with a few models compatible with Mars's observed range (H_{sur} within ~ 2.35–4.7).

It can be seen in Figure 11 that dynamo action is also hemispheric for models with multipolar magnetic fields. The snapshots of the magnetic and velocity fields of a reversing model (54 in Table 2) shown at a time when the dipole tilt is 34° (Figures 11(a) and (b)) and at a time when the tilt is 157° (Figures 11(c) and (d)) demonstrate that both toroidal and poloidal magnetic fields are mostly generated in the southern hemisphere at low latitudes and strong zonal flows are located in the southern hemisphere around the midlatitudes. This further corroborates that magnetic fields and the zonal flows are preferentially generated in the southern hemisphere in the multipolar dynamo regime. This suggests that the magnetic field is hemispheric whether the local field is represented by the intensity of a long time-averaged magnetic field or the time average of the magnetic field intensity.

We further investigate why the magnetic field transitions from a nonreversing, dipolar-dominated magnetic field to a multipolar field. In Figure 12 we plot the dipolarity, f_{Dip}, against the local Rossby number, Ro_l, for bottom-heated and internally heated dynamo models (i.e., models 1–37 in Table 1 and models 46–69 in Table 2) with varying VHF magnitudes. First, both bottom-heated and internally heated models with homogeneous heat flux patterns (enclosed by the rectangles in Figure 12) produce high dipolarities (i.e., $f_{dip} = 0.92 \pm 0.01$ for BH and $f_{dip} = 0.86 \pm 0.04$). The resulting dipolarity then decreases in both bottom-heated and internally heated models, as the Y_1^0 VHF perturbation magnitude increases (pointed in the direction of the arrows in Figure 12), until the field transitions to the multipolar regime. Furthermore, in the nonreversing, dipolar-dominated field regime, the local Rossby number is always lower in the models with non-zero VHF than in the corresponding homogeneous control model. There is also an overall trend of decreasing Ro_l with VHF magnitude, but it is not monotonic. This decrease of the local Rossby number is because the addition of the Y_1^0 VHF perturbation at the CMB pushes the velocity flows into larger length scales (see Figures 8(b) and (d), thus increasing the characteristic half-wavelength (π/l_u). In the multipolar regime, both bottom-heated and internally heated models produce small dipolarities ($f_{dip} \sim 0.1$), whereas the local Rossby number is comparatively higher. Models with higher Rayleigh numbers produce larger local Rossby numbers. Furthermore, bottom-heated dynamos seem to produce slightly higher local Rossby numbers than the internally heated dynamos. It is also worth noting that the local Rossby numbers in our multipolar models with non-zero VHF are lower than the critical local Rossby number ($\mathbf{Ro}_l = 0.1$) for transitions to multipolar fields found in homogeneously heated dynamos (Olson & Christensen 2006).
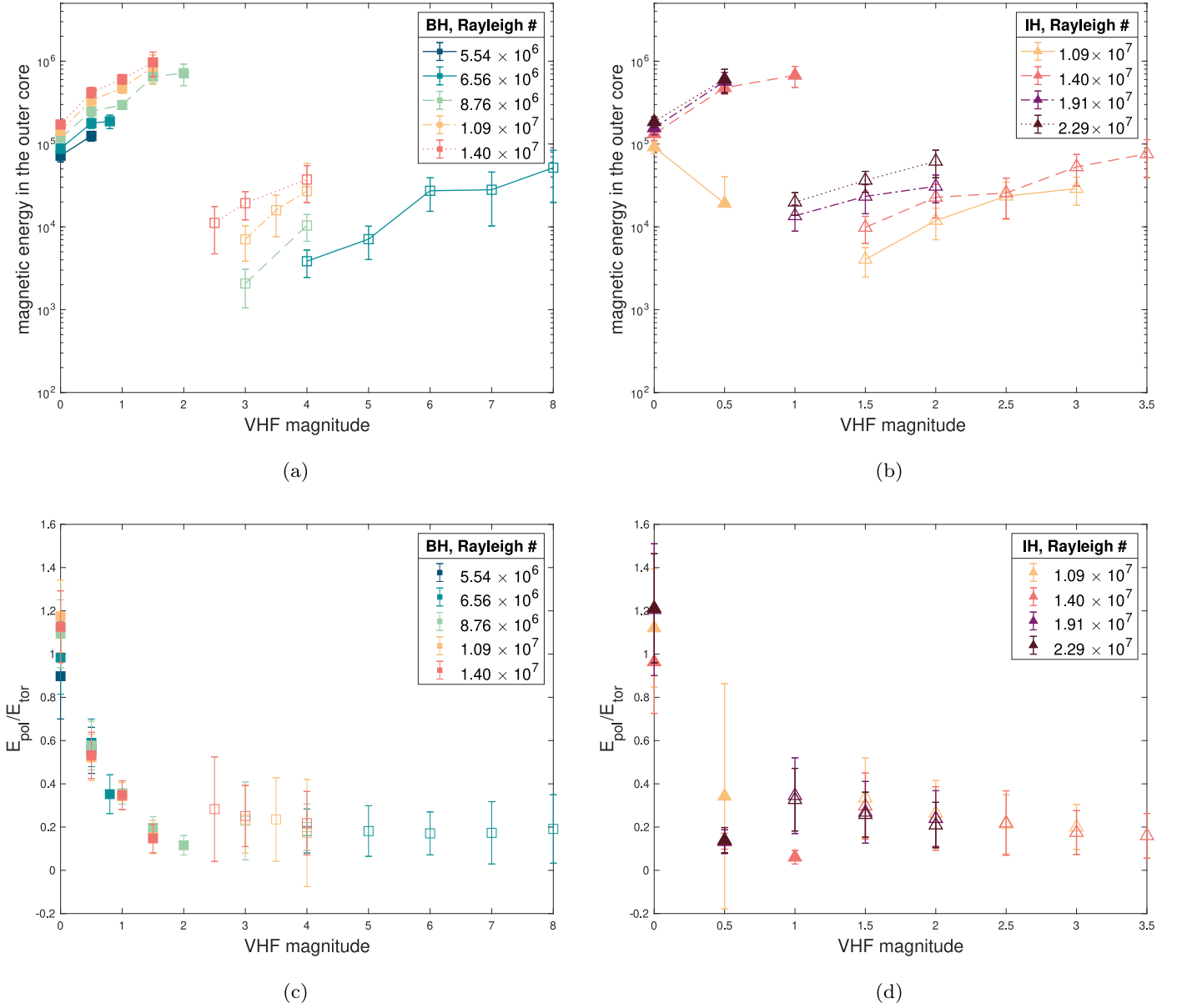
Figure 10. The magnetic energy as a function of the Y_1^0 VHF perturbation magnitude for models with (a) BH and (b) IH mechanisms, where open (filled) symbols represent nonreversing (reversing) models. The ratio of the poloidal to toroidal magnetic energy as a function of the Y_1^0 VHF perturbation magnitude for models with (c) BH and (d) IH mechanisms.

4. Discussion

Our study shows that the heating mechanism is an important determinant of the resulting dynamo behavior. Models powered by BH have a wider parameter window to produce nonreversing, dipolar-dominated magnetic fields than internally heated models. It is also worth noting that only the Rayleigh number is varying in both our bottom-heated and internally heated models and we have not varied other nondimensional parameters like the Ekman, Prandtl, or magnetic Prandtl numbers. However, the regime of a nonreversing, dipolar-dominated magnetic field likely depends on other nondimensional parameters such as Ekman, Prandtl, or magnetic Prandtl numbers (Christensen & Aubert 2006). It is possible that the ranges of the solution may be dependent on the choice of the parameter space. Future studies should investigate dynamo behaviors of various heating mechanisms with other varying nondimensional control parameters. At smaller VHF magnitudes, IH models produce

magnetic fields that are slightly more hemispheric than fields produced by BH models, consistent with the results in Hori et al. (2014). However, as we increase VHF magnitudes beyond the values used by Hori et al. (2014), we find that as VHF magnitude increases, both internally heated and bottom-heated models produce magnetic fields at very similar hemispfericity values. Furthermore, with increasing Y_1^0 VHF perturbations at the CMB, both bottom-heated and internally heated models produce nonreversing, dipolar-dominated magnetic fields that are concentrated in the southern hemisphere, which then transition to multipolar fields with frequently reversing dipole components under higher VHF perturbation magnitudes. Bottom-heated models can maintain a nonreversing, dipolar-dominated magnetic field at higher VHF perturbation magnitude. However, for internally heated models, the transition from a nonreversing, dipolar-dominated to a multipolar magnetic field occurs at comparatively smaller VHF
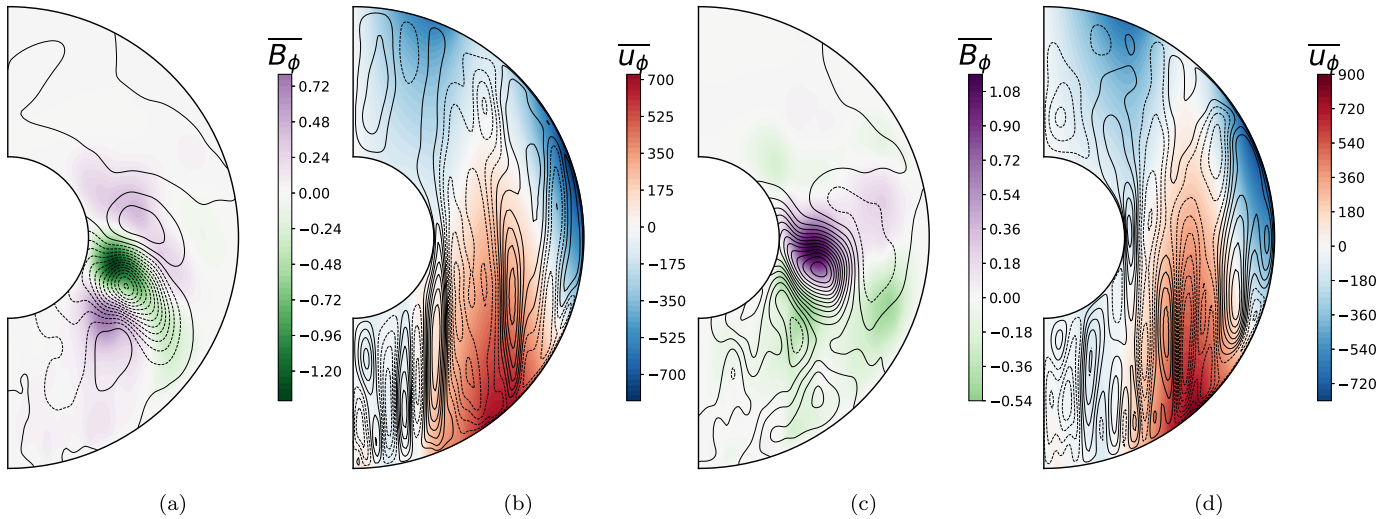
Figure 11. Snapshot of the axisymmetric toroidal (filled contours, $\overline{B_\phi}$) and poloidal (streamlines) magnetic field of a reversing dynamo model 54 when the dipole tilt is 34° (panel (a)) and 157° (panel (c)). Zonal flows (contours, $\overline{u_\phi}$) and meridional circulation (streamlines) of the same model when the dipole tilt is 34° (panel (b)) and 157° (panel (d)).
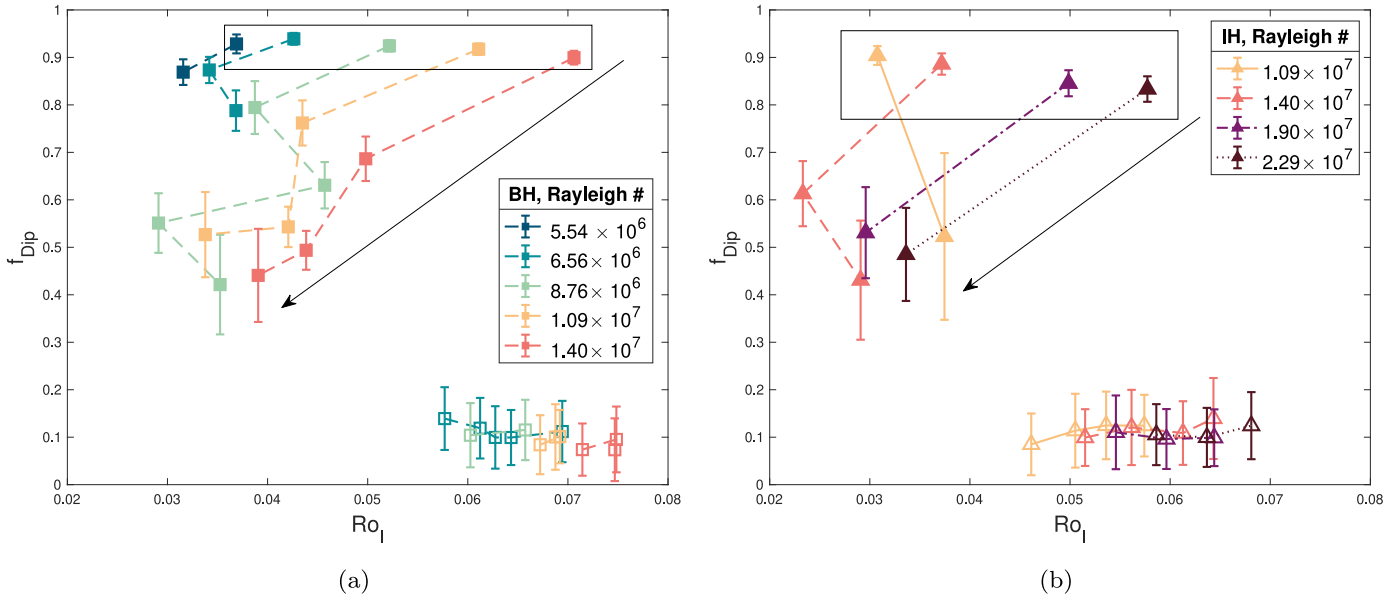

Figure 12. The dipolarity f_{Dip} vs. the local Rossby number Ro_l for models that are (a) bottom heated or (b) internally heated, averaged over 1 magnetic diffusion time. Open (filled) symbols represent nonreversing (reversing) cases. The rectangle marks the homogeneously heated models, and the arrow points in the direction of increasing VHF perturbation magnitudes.

magnitudes. Furthermore, the force balances of bottom-heated and internally heated dynamo models share the same ordering, albeit with slightly different magnitudes of forces, when compared with the same VHF magnitude in both nonreversing, dipolar-dominated and multipolar regimes.

In our study, both bottom-heated and internally heated models produce a few cases where the resulting magnetic hemisphericities are compatible with the observed Mars crustal magnetic field dichotomy ratio (2.35−4.7; Amit et al. 2011) in the multipolar regime. The magnetic field frequently reverses in the multipolar regime, while the fields are still preferentially generated in the southern hemisphere. However, the strength of the observed crustal magnetic field for a scenario where the field reverses frequently depends on the reversing period and the cooling times of the crustal rock in various geological units such as impact craters and lava flows. For example, if the

reversing period is much longer than the crustal rock cooling time, then the crust would record the instantaneous magnetic field at the time when it cools below the Curie temperature. However, if the reversing period is shorter than the cooling time, then the rocks may record magnetic fields with varying directions during the process of cooling and present net low-amplitude crustal field signatures at the surface. The reversing frequency in our models (Tables 1 and 2) gives an estimate of 1.8−3.4 kyr for the dipole reversal period ($T = \frac{\tau_\lambda}{2\,\mathrm{rev.freq.}}$, where τ_λ is the magnetic diffusion time that can be dimensionalized by $\tau_\lambda = r_o^2/\lambda$), taking $r_o = 1830\,\mathrm{km}$ as the outer core radius (Stahler et al. 2021) and $\lambda \sim 2\,\mathrm{m^2\,s^{-1}}$ (Roberts 2007) as the magnetic diffusivity of Mars's core materials, where similar material properties to Earth's core are assumed. This reversal period is at the same order of magnitude of estimates of

reversing periods found in Dietrich & Wicht (2013), which may be too short to obtain strong crustal magnetization, compared with typical cooling times in large intrusions (10^2 kyr; Cawthorn & Webb 2013), but is comparable to the cooling times of smaller geological signatures such as dike intrusions that could result in strong magnetizations. Additionally, other mechanisms might contribute to the observed dichotomy as well, e.g., localized distributions of magnetic-bearing minerals.

Recent tidal (Konopliv et al. 2020) and seismic (Stahler et al. 2021) measurements from the InSight mission found that the core density is relatively low, suggesting an excessive amount of light elements in Mars's core materials (Terasaki et al. 2019). This indicates the absence of a solid inner core of Mars at the present day. Furthermore, Mars's core may not have cooled down sufficiently enough to form a solid inner core throughout its history, although the possibility of an "iron snow" scenario where the core crystallizes from the top down cannot be excluded (Breuer et al. 2015). Future studies of Mars's ancient dynamo should also include full sphere modeling to investigate the effects of thermal perturbations at the CMB in the absence of an inner core. The lack of an inner core places constraints on the energy sources powering Mars's ancient dynamo, so that IH is more likely. In addition, this study of the effects of different heating mechanisms on dynamo behavior may provide insights on planets such as Earth and Mercury that have inner cores.

ORCID iDs

Chi Yan ⬤ https://orcid.org/0000-0001-8403-3288
Ankit Barik ⬤ https://orcid.org/0000-0001-5747-669X
Sabine Stanley ⬤ https://orcid.org/0000-0003-0469-4401
Jason S.-Y. Leung ⬤ https://orcid.org/0000-0001-7116-3710
Attilio Rivoldini ⬤ https://orcid.org/0000-0002-8626-9283

References

Acuña, M. H., Connerney, J. E. P., Ness, N. F., et al. 1999, Sci, 284, 790
Amit, H., Christensen, U. R., & Langlais, B. 2011, PEPI, 189, 63
Andrews-Hanna, J. C., Zuber, M. T., & Banerdt, W. B. 2008, Natur, 453, 1212
Arkani-Hamed, J. 2004, JGRE, 109, E09005
Banerdt, W. B., Smrekar, S. E., Banfield, D., et al. 2020, NatGe, 13, 183
Breuer, D., Rueckriemen, T., & Spohn, T. 2015, PEPS, 2, 39
Cawthorn, R. G., & Webb, S. J. 2013, Geo, 41, 687
Christensen, U. R., & Aubert, J. 2006, GeoJI, 166, 97
Christensen, U. R., Aubert, J., Cardin, P., et al. 2001, PEPI, 128, 25
Dietrich, W., & Wicht, J. 2013, PEPI, 217, 10
Elkins-Tanton, L. T., Parmentier, E., & Hess, P. 2003, M&PS, 38, 1753
Elkins-Tanton, L. T., Zaranek, S. E., Parmentier, E. M., & Hess, P. C. 2005, E&PSL, 236, 1
Fassett, C. I., & Head, J. W. 2011, Icar, 211, 1204
Frey, H., & Schultz, R. A. 1988, GeoRL, 15, 229
Grote, E., & Busse, F. H. 2000, PhRv, 62, 4457
Hood, L. L., Harrison, K. P., Langlais, B., et al. 2010, Icar, 208, 118
Hood, L. L., Zakharian, A., Halekas, J., et al. 2001, JGR, 106, 27825
Hori, K., Wicht, J., & Dietrich, W. 2014, P&SS, 98, 30
Hori, K., Wicht, Y., & Christensen, U. R. 2012, PEPI, 196, 32
Jakosky, B. M., Lin, R. P., Grebowsky, J. M., et al. 2015, SSRv, 195, 3
Johnson, C. L., Mittelholz, A., Langlais, B., et al. 2020, NatGe, 13, 199
Johnson, C. L., & Phillips, R. J. 2005, E&PSL, 230, 241
Ke, Y., & Solomatov, V. S. 2006, JGRE, 111, E10001
Khan, A., Sossi, P. A., Liebske, C., Rivoldini, A., & Giardini, D. 2022, E&PSL, 578, 117330
Konopliv, A. S., Park, R. S., Rivoldini, A., et al. 2020, GeoRL, 47, e90568
Landeau, M., & Aubert, J. 2011, PEPI, 185, 61
Langlais, B., Thébault, E., Houliez, A., Purucker, M., & Lillis, R. 2019, JGRE, 124, 1542
Lillis, R. J., Frey, H. V., & Manga, M. 2008, GeoRL, 35, L14203
Lillis, R. J., Robbins, S., Manga, M., Halekas, J. S., & Frey, H. V. 2013, JGRE, 118, 1488
Milbury, C., Schubert, G., Raymond, C. A., Smrekar, S. E., & Langlais, B. 2012, JGRE, 117, E10007
Mittelholz, A., Johnson, C. L., Feinberg, J. M., Langlais, B., & Phillips, R. J. 2020, SciA, 6, eaba0513
Mohit, P. S., & Arkani-Hamed, J. 2004, Icar, 168, 305
Monteux, J., Amit, H., Choblet, G., Langlais, B., & Tobie, G. 2015, PEPI, 240, 114
Nimmo, F., & Gilmore, M. S. 2001, JGR, 106, 12315
Nimmo, F., Hart, S. D., Korycansky, D. G., & Agnor, C. B. 2008, Natur, 453, 1220
Ojha, L., Karunatillake, S., Karimi, S., & Buffo, J. 2021, NatCo, 12, 1754
Olson, P., & Christensen, U. R. 2006, E&PSL, 250, 561
Quesnel, Y., Sotin, C., Langlais, B., et al. 2009, E&PSL, 277, 184
Roberts, J. H., & Zhong, S. 2006, JGRE, 111, E06013
Roberts, P. 2007, in Treatise on Geophysics, ed. G. Schubert (Amsterdam: Elsevier), 67
Schaeffer, N. 2013, GGG, 14, 751
Simitev, R., & Busse, F. H. 2005, JFM, 532, 365
Solomon, S. C., Aharonson, O., Aurnou, J. M., et al. 2005, Sci, 307, 1214
Stanley, S., & Mohammadi, A. 2008, PEPI, 168, 179
Stahler, S. C., Khan, A., Banerdt, W. B., et al. 2021, Sci, 373, 443
Steele, S. C., Fu, R. R., Ermakov, A. I., et al. 2022a, LPSC, 53, 1769
Steele, S. C., Fu, R. R., Volk, M. W. R., et al. 2022b, LPSC, 53, 1764
Terasaki, H., Rivoldini, A., Shimoyama, Y., et al. 2019, JGRE, 124, 2272
Vervelidou, F., Lesur, V., Grott, M., Morschhauser, A., & Lillis, R. J. 2017, JGRE, 122, 2294
Weiss, B. P., Vali, H., Baudenbacher, F. J., et al. 2002, E&PSL, 201, 449
Wicht, J. 2002, PEPI, 132, 281
Wilhelms, D. E., & Squyres, S. W. 1984, Natur, 309, 138
Zhong, S., & Zuber, M. T. 2001, E&PSL, 189, 75